Journal of Structural Geology 195 (2025) 105394

Contents lists available at ScienceDirect

Journal of Structural Geology

journal homepage: www.elsevier.com/locate/jsg

Strain partitioning and fault interaction during the 2023 M_w 6.8 Al-Haouz earthquake, Western High Atlas, Morocco

F. Carboni [a,b,*], M. Occhipinti [b,c], R. Lanari [d], F. Medina [e], T.-E. Cherkaoui [i], R. Gaspari [c], C. Faccenna [f,g], C. Chiarabba [h], M. Porreca [b,c]

[a] Institute of Earth and Environmental Sciences (Geology), Albert-Ludwigs-University Freiburg, Freiburg, Germany
[b] CRUST - Interuniversity Centre for 3D Seismotectonics with Territorial Applications, Chieti, Italy
[c] Department of Physics and Geology, University of Perugia, Perugia, Italy
[d] Institute of Geosciences and Earth Resources, National Research Council of Italy (CNR), Florence, Italy
[e] Moroccan Association of Geosciences, Commission of Natural Hazards, Rabat, Morocco
[f] Department of Science, Roma Tre University, Rome, Italy
[g] GFZ-German Research Centre for Geosciences, Potsdam, Germany
[h] National Institute of Geophysics and Vulcanology (INGV), Rome, Italy
[i] University Mohammed V, Rabat, Morocco

ARTICLE INFO

Keywords:
2023 Mw 6.8 Al-Haouz earthquake
Western high atlas
DInSAR
Coulomb stress
Triangular elastic dislocation modelling

ABSTRACT

This study employs a multidisciplinary approach to identify the seismogenic fault responsible for the Mw 6.8 Al Haouz earthquake of September 8, 2023, in the Western High Atlas, Morocco. In addition, considering the oblique slip dynamics and strain partitioning characteristic of the region, the study investigates potential interactions between fault systems at depth. Our new relocation of the mainshock confirms the depth of the mainshock at ca. 28 km, while our relocated aftershocks reveal clusters concentrated near the Tizi n'Test fault (TnTf) and aligned patterns consistent with fault-controlled seismicity. Focal mechanisms of the mainshock indicate a compressive event involving two nodal planes: a high-angle NW-dipping plane and a low-angle SW-dipping plane. DInSAR analysis generated displacement maps for vertical and horizontal (E-W) components, revealing an asymmetric SW-verging uplift bounded, in the south, by the NW-dipping Tizi n'Test fault (TnTf). The Triangular Elastic Dislocation (TDE) method is conducted to simulate complex faults geometries using geological data and focal mechanism solution.

The NW-dipping TnTf shows a better fit with the observed deformation compared to the SW-dipping Jebilet Thrust (JTt), which contributed with a minor role. Coulomb stress changes calculated from the TDE model correlates with aftershocks distribution, further supporting the TnTf as the causative fault, with a partial influence of the JTt.

Our findings emphasize the value of integrating geodetic observations with advanced modelling to enhance the understanding of the seismotectonic framework, offering a refined reconstruction of the Western High Atlas's deformation processes during the 2023 Al Haouz earthquake.

1. Introduction

On September 8th, 2023, at 23:11 DST, a Mw 6.8 earthquake struck the Western High Atlas Mountains (WHA) in Morocco, representing one of the most significant seismic events in recent decades (Cherkaoui and El Hassani, 2012; Jabour et al., 2004; Peláez et al., 2007). The main event occurred 73 km southwest of Marrakesh, in the Al-Haouz province within the Marrakesh-Safi region (hence the medias denomination of Al-Haouz earthquake), at an unusual crustal depth. Initial estimations of the focal depth were given by the U.S. Geological Survey (USGS) at 30.5 km, by the Centre Sismologique Euro-Méditerranéen (CSEM) at 26 km, and by the Global Centroid-Moment-Tensor Project (Global CMT) at 23.8 km. More recently, Bondár et al. (2024) relocated the mainshock at shallower depths ranging between 9 and 14 km depending on the relocation method.

The epicentral area is located in the WHA, part of a tectonically

* Corresponding author. Institute of Earth and Environmental Sciences (Geology), Albert-Ludwigs-University Freiburg, Freiburg, Germany.
E-mail address: filippocarboni@ymail.com (F. Carboni).

https://doi.org/10.1016/j.jsg.2025.105394
Received 14 October 2024; Received in revised form 28 February 2025; Accepted 4 March 2025
Available online 6 March 2025

complex belt characterized by low strain rates (Koulali et al., 2011; Serpelloni et al., 2007; Skikra et al., 2025b) and low seismicity (Cherkaoui and El Hassani, 2012; Peláez et al., 2007; Sébrier et al., 2006; Soumaya et al., 2018). The WHA consist of a double-verging orogen formed during the Cenozoic convergence of the African (Nubian) plate towards the Eurasian plate, characterized by a crustal thickness of 32–40 km (Mancilla and Diaz, 2015; Spieker et al., 2014; Timoulali et al., 2015). The belt is mainly driven by transpressional tectonics, characterized by two main fault groups (Skikra et al., 2025b and references therein): transpressive faults along the orogenic axis and thrust systems along the orogenic margins (Fig. 1). Focal mechanism solutions from the USGS and Global CMT indicate that the earthquake can be attributed to both a low-angle SW-dipping or a high-angle NW-dipping fault plane. Both planes are associable to either a low angle thrust or to a high angle transpressive fault, respectively.

Although the magnitude of the mainshock is significant, no surface coseismic ruptures were recognized in the field, possibly due to the high depth of the earthquake hypocentre, leaving uncertainties on the possible fault responsible for the Al-Haouz earthquake. These uncertainties are also related to the lack of subsurface data, which is commonly the key to unravel faults geometry at depth in seismically active regions (e.g., Barchi et al., 2021; Bello et al., 2022; Carboni et al., 2024; Ferranti et al., 2024; Ercoli et al., 2023; Porreca et al., 2018). Therefore, the main techniques to unravel the seismotectonic

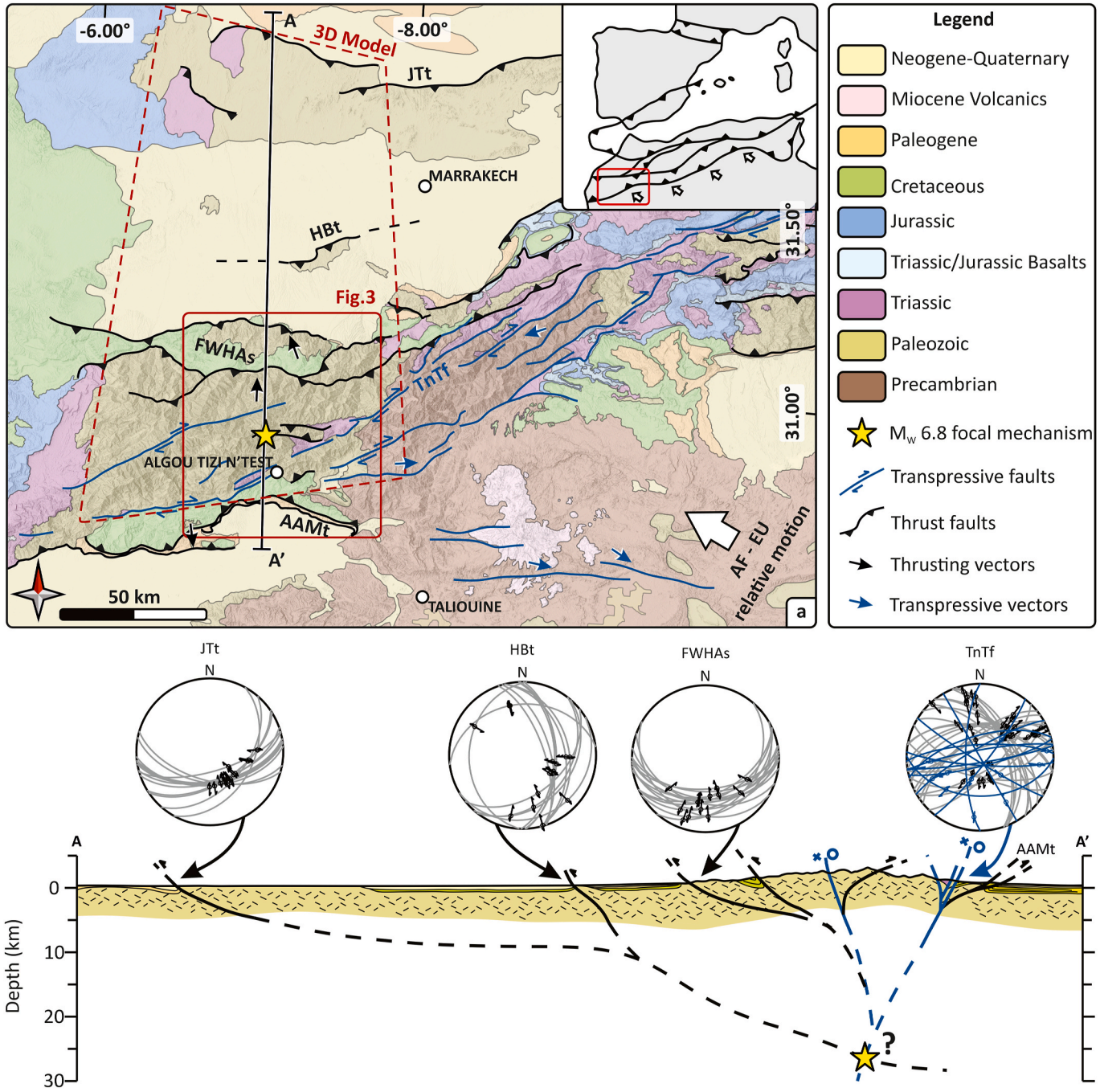

Fig. 1. (**a**) Location of the study area and simplified geological map of the Western High Atlas (after Lanari et al., 2020a). JTt: Jebilet thrust; HBt: Haouz Basin thrust; FWHAs: Far Western High Atlas system; TnTf: Tizi n'Test fault; AAMt: Anti Atlas Major thrust. (**b**) Simplified geological cross section showing the main tectonic structures and the related kinematic indicators by Lanari et al. (2020a).

framework of this earthquake, rely mainly on field geology, geodetic data and modelling; however, these techniques are not commonly integrated. Yeck et al. (2023), based on slip inversion, suggests a blind structure as the causative fault. Similarly, Malusà et al. (2024), based on extensive fieldwork, indicate a newly formed blind structure as a possible causative fault. Levandowski (2023) suggests how the two planes indicated by the focal mechanism are geologically plausible for the area: the gentle SW-dipping plane aligns with stress inversion data, while the steep NW-dipping plane fits finite fault modelling. Touati et al. (2024), from a combination of DInSAR analysis and seismic wave data, supports the high-angle plane hypothesis. Skikra et al. (2025a) examine the Al-Haouz earthquake by using seismological data, frequency-magnitude distribution analysis and GNSS information, supporting the TnTf as the seismogenic fault. Further support to the NW-dipping high-angle solution is given by Huang et al. (2024), whose DInSAR observations are used as a basis to perform probabilistic Bayesian inversion, determining a seismogenic fault plane centred at 26 km depth, aligned with the TnTf. Yagi et al. (2024) also preferred the high-angle NW-dipping plane to perform their teleseismic P-wave analysis. Nouayti et al. (2024), which integrate geological data and aftershocks distribution with magnetic and gravity surveys, suggests the TnTf as the causative structure, also supporting a more complex geodynamic framework. Conversely, Cheloni et al. (2024) favours the low-angle SW-dipping plane, based on finite fault modelling integrated with hypocentre localization, gravity, and heat flow data, linking that with the North Atlas Fault (i.e., FWHAs). In sustaining a similar hypothesis, Wu et al. (2024) exploited DInSAR and Pixel Offset Tracking (POT) methods, integrated with the strain model-variance component estimation method (SM-VCE).

Despite these studies, the current research on the Al-Haouz earthquake remains limited to identifying the causative fault, without accounting for the geological complexities of the epicentral area. To further clarify debated aspects regarding the seismogenic fault and its relationship with other existing faults, we integrate existing geological data, an updated relocation of the mainshock and aftershocks, DInSAR data, Triangular Elastic Dislocation (TDE) modelling of planar and irregular faults. The DInSAR method is used to derive the coseismic surface deformation field resulting from the 2023 Al-Haouz earthquake. The Triangular Elastic Dislocation modelling is used to reproduce the coseismic deformation by modelling planar (i.e., nodal planes form the focal mechanism) and irregular fault (i.e., outcropping and mapped faults) solutions at depth. The modelling enables the simulation of deformation on one fault as a result of slip induced on another, highlighting potential interactions and stress transfer between faults. Coulomb stress changes are derived from TDE to observe the distribution of the updated relocated 259 aftershocks, according to the good agreement of aftershocks distribution with the positive Coulomb stress changes (e.g., Harris, 1998; Steacy et al., 2005). From this correlation, we propose that the Tizi n'Test system is the likely causative for the 2023 Al-Haouz earthquake. We also open new insights on possible locally induced reactivations of faults at depth (i.e., JTt), accommodating oblique convergence with strain partitioning. In such way, it is possible to evaluate not only the kinematics of the TnTf but also the contribution of the JTt, identifying an interplay between these two faults and formulating a novel detailed reconstruction of the seismotectonic framework of the 2023 Al-Haouz earthquake and the WHA.

2. Geology of the Western High Atlas

The WHA (Fig. 1a) represents the westernmost and highest portion of the High Atlas Mountains in Morocco, an orogen elongated for 650 km from WSW to ENE. The numerous tectonic structures oriented from WSW-ENE to SW-NE composing the WHA are associated with a wide dextral shear zone along the entire North Africa (Dias et al., 2011; Soumaya et al., 2018). The shear zone is related to transpressional tectonics (Ellero et al., 2012; Lanari et al., 2020b) as a consequence of oblique convergence of the African Plate relatively to the Eurasian Plate, oriented NW-SE (DeMets et al., 1994, 2015; Dewey et al., 1989; Serpelloni et al., 2007). The main tectonic structures within the area are, from north to south (Fig. 1a) : i) the SSW-dipping Jebilet front thrust (JTt), which confines the WHA in the north with an E-W trend; ii) the SSE-dipping Haouz Basin thrust (HBt), also known as the Guemassa fault, crossing the Haouz Basin with a ENE-WSW direction (Fekkak et al., 2018) and here interpreted as a secondary splay ramping out from the JTt; iii) the S-dipping Far Western High Atlas thrust system (FWHAs), composed a series of thrusts oriented E-W; iv) the NNW-dipping Tizi n'Test (TnTf), striking SW-NE; v) the N-dipping Anti Atlas Major thrust (AAMt) mainly oriented E-W. The geological cross section (Fig. 1b) shows the Quaternary kinematic indicators obtained in the field (Lanari et al., 2020a, 2020b) and the interpretation of the major tectonic structures at depth. The kinematic indicators of the thrusts (JTt, HBt, FWHAs) show a main dip-slip motion, with an overall northward transport direction. The kinematic indicators of the TnTf are more complex and show both pure dextral strike-slip and dextral transpressive kinematics.

The building of the WHA is part of the Alleghenian-Variscan orogeny and is primarily controlled by a major WSW-ENE to E-W dextral shear zone (Dias et al., 2011). Key structures have governed the evolution of the mountain belt, among which the TnTf is considered the primary controlling fault as a major suture (Dias et al., 2011; Mattauer et al., 1972). Additionally, second-order faults, interpreted as Riedel shears of the major faults, are present in the region (Dias et al., 2011).

Since the Permian, extension linked to the breakup of Africa led to a crustal thinning and the formation of a rift basin during the Triassic and Jurassic (Arboleya et al., 2004; Beauchamp et al., 1996; Laville and Pique, 1991; Teixell et al., 2003). During the Cenozoic, the tectonic inversion of the rift basin (Ellero et al., 2020; Gomez et al., 2000; Teixell et al., 2003) led to the reactivation of several tectonic structures belonging to the Variscan orogeny and inherited from the Triassic – Jurassic period, among which is the TnTf. The reactivation occurs in a transpressive context, characterized by strain partitioning among thrust and transpressive faults (e.g., Delcaillau et al., 2011; Ellero et al., 2012, 2020; Fekkak et al., 2018; Lanari et al., 2020a; Skikra et al., 2025b). The strongest tectonic influence derives from right-lateral transpressive faults with reverse component, with the TnTf being the most prominent expression (Delcaillau et al., 2011; Ellero et al., 2012). The ongoing transpression started during the late Eocene (Frizon de Lamotte et al., 2009; Leprêtre et al., 2015, 2018), with the main phase initiated in the middle – late Miocene (Balestrieri et al., 2009; Barbero et al., 2011; Domènech et al., 2016; Ghorbal et al., 2008; Missenard et al., 2008; Lanari et al., 2020b, 2023a), persisting at lower rates until recent times (Arboleya et al., 2008; Tesòn and Teixell, 2008).

Cenozoic exhumation rates, derived from thermochronological analysis, are estimated to range from 0.1 to 0.2 km/Ma, with faster rates in the south (Lanari et al., 2020a, 2020b). The WHA high topography is in contrast with the modest crustal thickening (Teixell et al., 2003), suggesting that multiple mechanisms other than crustal isostasy (i.e., deformation) must be considered (Babault et al., 2008; Lanari et al., 2023b; Missenard et al., 2006; Teixell et al., 2005). Indeed, since late Miocene, deformation and exhumation occurred coevally with surface uplift and anorogenic volcanism (e.g. Clementucci et al., 2023; Lanari et al., 2020a; Bouiflane et al., 2024). However, Lanari et al. (2023b) demonstrated that, even if exhumation rates depict a short-wavelength signature (e.g., tectonics) rather than a large-wavelength one (e.g., mantle dynamic), the late Miocene mantle upwelling played a key role in structuring the High Atlas (e.g., Teixell et al., 2005). Lanari et al. (2023b) proposed that the mantle impingement eroded the lower lithosphere, resulting in crustal weakening, which in turn enhanced crustal deformation and exhumation; to this it is also linked an overall regional surface uplift widespread recorded in Morocco (e.g. Babault et al., 2008; Clementucci et al., 2023; 2024). Conversely, Malusà et al. (2024) propose a minor role of asthenospheric upwelling, suggesting how the

region would be more strongly controlled only the by oblique-convergence of the African and Eurasian plates.

2.1. Seismological framework

The High Atlas are characterized by a general widespread moderate seismicity, with $M_w < 5$ and epicentres aligned in a NE-SW trend, parallel to the WHA direction (Bensaid et al., 2011; Cherkaoui, 1991; Cherkaoui and El Hassani, 2012; Sébrier et al., 2006). According to seismicity maps of Morocco, this region is characterized by low seismic activity. This could be attributed to the lack of proximity to seismic monitoring stations prior to the network's expansion, causing low-magnitude earthquakes (<3.5) to go undetected (Cherkaoui, 1991; Medina and Cherkaoui, 1991).

Although only a few focal mechanisms are truly reliable, they indicate an overall compressional regime with NNW-trending P-axes (Sébrier et al., 2006), in agreement with the average NW-directed Africa-Eurasia convergence as indicated by GNSS data (Serpelloni et al., 2007). Since 1900, only nine seismic events larger than M_w 5 occurred. In particular, two seismic events of M_w 5.5 have been recorded in the eastern Anti-Atlas region (e.g., Cherkaoui, 1991; Medina and El Alami, 2006; Peláez et al., 2007; Sébrier et al., 2006). The largest earthquake ever recorded in the entire region corresponds to the February 29th, 1960 Agadir earthquake sequence, with a ~6.0 M_w (Cherkaoui, 1991; Cherkaoui and Medina, 1988; Duffaud et al., 1962; Meghraoui et al., 1999; Mourabit et al., 2014; Timoulali and Meghraoui, 2011). Considering this scenario, the occurrence of the Mw 6.8 Al-Haouz earthquake represents a singular event to highlight the peculiarity of intracontinental earthquakes.

3. Data and methods

3.1. Seismicity re-location

The aftershocks following the Mw 6.8 mainshock are initially manually processed to achieve greater accuracy in location. Subsequently, we obtain all the seismic station data (P and S first arrival times) from the two Moroccan networks (the Scientific Institute of Mohammed V University in Rabat and the National Centre for Scientific and Technical Research in Rabat). To these data, we add those from the Spanish and Portuguese seismic networks. We process 259 aftershocks from 09.09.2023 to 30.01.2024, among which 202 occurred during 09.09.2023 (Table S1). The new aftershock catalogue consist of, excluding the mainshock, 23 events with $M_w \geq 4$, 72 events of $4 < M_w \leq 3$, 159 events of $3 < M_w \leq 1$, and 4 events of $M_w < 1$. For the localization of aftershocks, we use the HypoInverse program (Klein, 2002) with a velocity model, in which Vp/Vs = 1.77 (Table 1). The adopted Vp velocities are in conformity with those determined from recent studies in the area (Spieker et al., 2014; Timoulali and Meghraoui, 2011).

To establish a correlation between seismicity and tectonics, as well as to ensure a precise and representative analysis, we filter the list of aftershocks based on the following criteria in the context of a permanent seismic network: i) NS ≥ 5; ii) RMS ≤2.0 s; iii) ERH and ERZ ≤10 km; iv) GAP ≤180°. NS refers to the number of seismic stations that recorded the event; a minimum of 5 stations ensures sufficient data for accurately determining the earthquake location and characteristics. RMS (Root Mean Square error) is a measure of the residual differences between observed and calculated arrival times of seismic waves; values ≤ 2.0 s indicates a reasonably good best fit between the calculated and the observed location of the earthquake, suggesting a reliable solution. ERH and ERZ are the horizontal and vertical location uncertainties of the earthquake hypocentre, respectively; values ≤ 10 km indicate a good accuracy and precision for the earthquake location both horizontally and vertically, considering the network geometry and distance between seismic stations. GAP refers to the largest azimuthal gap in station coverage around the earthquake, measured in degrees; GAP ≤180° ensures that stations are well-distributed around the earthquake, minimizing location errors caused by poor station geometry.

Table 1
Velocity model used for the re-localization.

Velocity model					
Vp (km/s)	6	6.8	8	8.2	8.3
Depth (km)	0	15	36	80	200

3.2. DInSAR

The dataset used in this work is obtained from Sentinel-1A SLC IW products and consists of two pairs of SAR images, retrieved from 18.08.2023 to 15.09.2023, coupled to generate two interferometric pairs. Data from the 03.09.2023 and 15.09.2023 are collected over ascending orbit along track 45, while data from the 18.08.2023 and the 11.09.2023 are collected over descending orbit along track 154. Since the radar sensor in Sentinel-1 acquires the image using the C-band of the electromagnetic spectrum (λ = 5.6 cm) through the Interferometric Wide (IW) swath acquisition mode, the spatial resolution of the SAR image is 2,7 × 22 m to 3,5 × 22 m (range x azimuth) with a vertical accuracy of $\lambda/2$ (ca. 3 cm), and a vertical error of $\lambda/8$ (ca. 0.7 cm) (Bignami et al., 2019).

The application of the DInSAR technique (Gabriel et al., 1989; Massonnet and Feigl, 1998), allows to obtain a detailed coseismic deformation, providing a better understanding of the mechanisms behind strong seismic events, especially if integrated with field data, further geodetic observations and modelling. This approach is extensively applied to several worldwide seismic events (e.g., Carboni et al., 2022; Lanari et al., 2010; Lavecchia et al., 2016; Papadopoulos et al., 2021; Tondi et al., 2021; Valerio et al., 2020) to identify the seismogenic faults and/or the coseismic deformation field.

In this work, the DInSAR processing chain is performed using an in-house developed script, named SNAP2DQuake (Occhipinti et al., 2024), which is written in Python and based on the library "esa_snappy" furnished by the SNAP software (ESA). The script reproduces automatically all the steps previewed in the DInSAR workflow, computing the differential interferograms (Figs. S1a and b) and the corresponding LOS movement maps (Figs. S1c and d) to generate the vertical and horizontal displacement field maps (Occhipinti et al., 2024), named VDm and HDm, respectively. The processing is performed at the Sentinel-1A full spatial resolution until the interferogram generation, after which a multi-look operation is applied to increase the signal-to-noise ratio; finally, the SRTM-3 arcsec Digital Elevation Model (DEM) is used to remove the topographic phase contribution. The final VDm and HDm, retrieved through a proper phase unwrapping operation of the interferograms, have a spatial resolution of ca. 27 m/px.

3.3. Triangular Elastic Dislocation modelling

Elastic dislocation modelling is capable of calculate displacement, induced surface deformation, strains and stresses linked to faulting from earthquakes occurrence (e.g., Burgmann et al., 2002; Lavecchia et al., 2016; McGuire and Segall, 2003; Okada, 1985, 1992; Savage and Burford, 1973). From it, the Coulomb stress changes can be determined in the area surrounding the active seismogenic modelled fault, which is demonstrated to be mostly in agreement with aftershocks distribution (e.g., Harris, 1998; Steacy et al., 2005). Furthermore, the modelling allows to perform a Slip Tendency analysis, which calculates the likeliness of a plane to slip in response of the ratio of the resolved shear stress to normal stress. We perform Triangular Elastic Dislocation (TDE) modelling using the Fault Response Modelling tool in Move (PE Limited) software, which is based on the algorithms by Meade (2007). Such modelling technique, differently from a classical stress inversion, allows to model irregular fault geometries along both dip and strike as

triangular mesh. The tool allows to set a range of mechanical and kinematic parameters; the mechanical parameters of the deformed rock volume are chosen assuming an overall granitic composition (e.g., Domènech et al., 2016; Lanari et al., 2020a,b), following common mechanical values (e.g., Qin et al., 2020; Zhang et al., 2024). They include Poisson' ratio, Young modulus, coefficient of friction, internal friction angle and cohesion. The kinematic parameters allow to specify detailed slip directions, amount of slip, rake and slip tapering to obtain also asymmetric slip gradients such as oblique elliptical areas of slip. The chosen parameters are shown in Table 2.

The source parameters (strike, dip, rake) used in this work are taken from the nodal planes calculated by the USGS (Table 2), while the location of the mainshock is given by our new re-localization. We initially model two simple planes in accordance with the USGS: one high-angle NNW-dipping plane oriented N 255° 69° with a rake of 69° and one low-angle SW-dipping plane oriented N122° 29° with a rake of 132°. Subsequently, we model the main regional faults in agreement with the nodal planes and mainshock location, which are the JTt and the TnTf (Fig. 1b). Fault modelling is conducted using surface geological data (e.g., fault traces) and their interpreted continuation at depth, passing through the hypocentre. The subsurface fault geometry is reconstructed based on published interpretations, the mainshock location and aftershocks distribution. In this study, the JTt and TnTf faults are modelled to represent the two nodal planes. The JTt is modelled with a flat-ramp-flat geometry, where the connecting ramp is linked to the HBt thrust, here interpreted as a secondary splay of the JTt. Such geometry reflects the heterogeneous mechanical stratigraphy and multiple detachment levels described by Missenard et al. (2007). Although there are no further constraint to extend the JTt up to beneath the WHA, a similar geometry is already suggested by Ellero et al. (2012, 2020). Both the JTt and the HBt are considered together as a linked fault system. Conversely, the TnTf is modelled with a steep geometry, consistent with structural data from field studies (Ellero et al., 2012, 2020; Malusà et al., 2024; Missenard et al., 2007; Lanari et al., 2020a, 2020b, 2023b).

The vertical deformation maps generated through TDE modelling are compared with the DInSAR deformation to identify the best-fit model and to determine the possible causative fault. Since the Al-Haouz earthquake was triggered by reverse faulting with a negligible strike-slip motion, the comparison focused exclusively on the vertical component of the coseismic deformation (VDm). The Coulomb derived from the TDE models is compared with the distribution of the newly re-localized aftershocks and faults' locations, providing insights into fault activity and potential induced reactivations. Further to that we exploit the possibility of an induce slip of the JTt in response to the activity of the TnTf using the Coulomb Stress change and the Slip Tendency analysis.

4. Results

4.1. Seismicity distribution

The re-located mainshock, now N 30.96° W 8.44° at 28.3 km depth, and the re-located aftershocks are more concentrated in proximity of the TnTf and the AAMt, gradually becoming sparser toward the north and south (Fig. 2a). In the north, a scattered cluster shows slight northeast elongation, whereas in the south, a few well-aligned aftershocks trend southeast. All the aftershocks are plotted into the two sections BB' and CC' (Fig. 2), oriented based on the events distribution, to visualize the distribution in respect to the faults; projecting only a buffer relatively closed to the sections would result in too few events. At depth (Fig. 2b and c), seismicity spans from very shallow levels (less than 2 km) down to approximately 35 km, confined between the JTt and the AAMf. The sections of Fig. 2b and c shows two different patterns of seismicity: a dense shallow distribution and a more dispersed deep cluster. We also recognize a general temporal migration of the aftershock towards the north (Fig. 2a) even if it is represented by few events. In particular, the shallow aftershocks are densely distributed from 2 to 12 km of depth and bounded by the footwall of AAMf and the antithetic transpressive fault of the TnTf. Further north, a seismic gap for this shallow distribution is evident until the FWHAs external thrust. The deep aftershocks are sparsely located between 10 and 35 km, including the mainshock, and are grouped between the FWHAs external thrust and the JTt, as upper and lower boundary structures respectively; the cluster is then well confined in the north by the HBt. Other few aftershocks occurred below the JTt.

4.2. DInSAR

The VDm (Fig. 3a) shows an evident general uplift in correspondence of the mainshock, with a maximum value of ca. 22 cm in the northeast of the re-localized epicentre. The deformation extends for ca. 50 km in the N-S direction and more than 60 km long in the E-W direction. The deformed area, containing a series of thrusts and transpressive faults (e.g., Domènech et al., 2016; Ellero et al., 2012; Fekkak et al., 2018; Lanari et al., 2020b), drastically decreases southwards in correspondence with the TnTf, while the decrement is gentler going northwards, until the FWHAs external thrust. Thus, the VDm appears constrained between these two main fault systems. The deformation field, recalls an antiform geometry, whose axial plane is basically E-W oriented. The antiform shows a steeper SE-dipping front-limb and a long shallower NW-dipping back-limb, suggesting an asymmetric SSE-vergence.

The HDm (Fig. 3b) shows two lobes representing a movement of ca. 9 cm towards both the west and the east. The overall deformed area is again constrained between the FWHAs in the north and the TnTf in the south. The boundary of the two lobes falls almost in correspondence with the maximum uplift, i.e., the core of the VDm antiform, suggesting

Table 2
Mechanical and kinematic modelling parameters including the original nodal planes from USGS, the two modelled simple planes, the irregular TnTf and JTt. The slip ellipsoid refers to the orientation (i.e., elongation) of the asymmetric area of given slip.

Nodal plane 1				**Nodal plane 2**			
Strike/Dip	**Rake**	**Mw**	**Depth**	**Strike/Dip**	**Rake**	**Mw**	**Depth**
255° 69°	69°	6.8	28.3	122° 29°	132°	6.8	28.3
L x W	**Slip**	**Slip ellipsoid**	**Depth**	**L x W**	**Slip**	**Slip ellipsoid**	**Depth**
22 × 18 km	2.4 m	–	28.3	22 × 18 km	2.6 m	–	28.3
TnTf				**JTt**			
L x W	**Slip**	**Slip ellipsoid**	**Depth**	**L x W**	**Slip**	**Slip ellipsoid**	**Depth**
38 × 23 km	2.3 m	300°	28.3 km	41 × 28 km	3 m	48°	28.3 km
Mechanical Parameters							
Poisson's Ratio	**Young's Modulus**		**Friction Coefficient**		**Internal Friction Angle**		**Cohesion**
0.25	30 MPa		0.6		31°		25 MPa

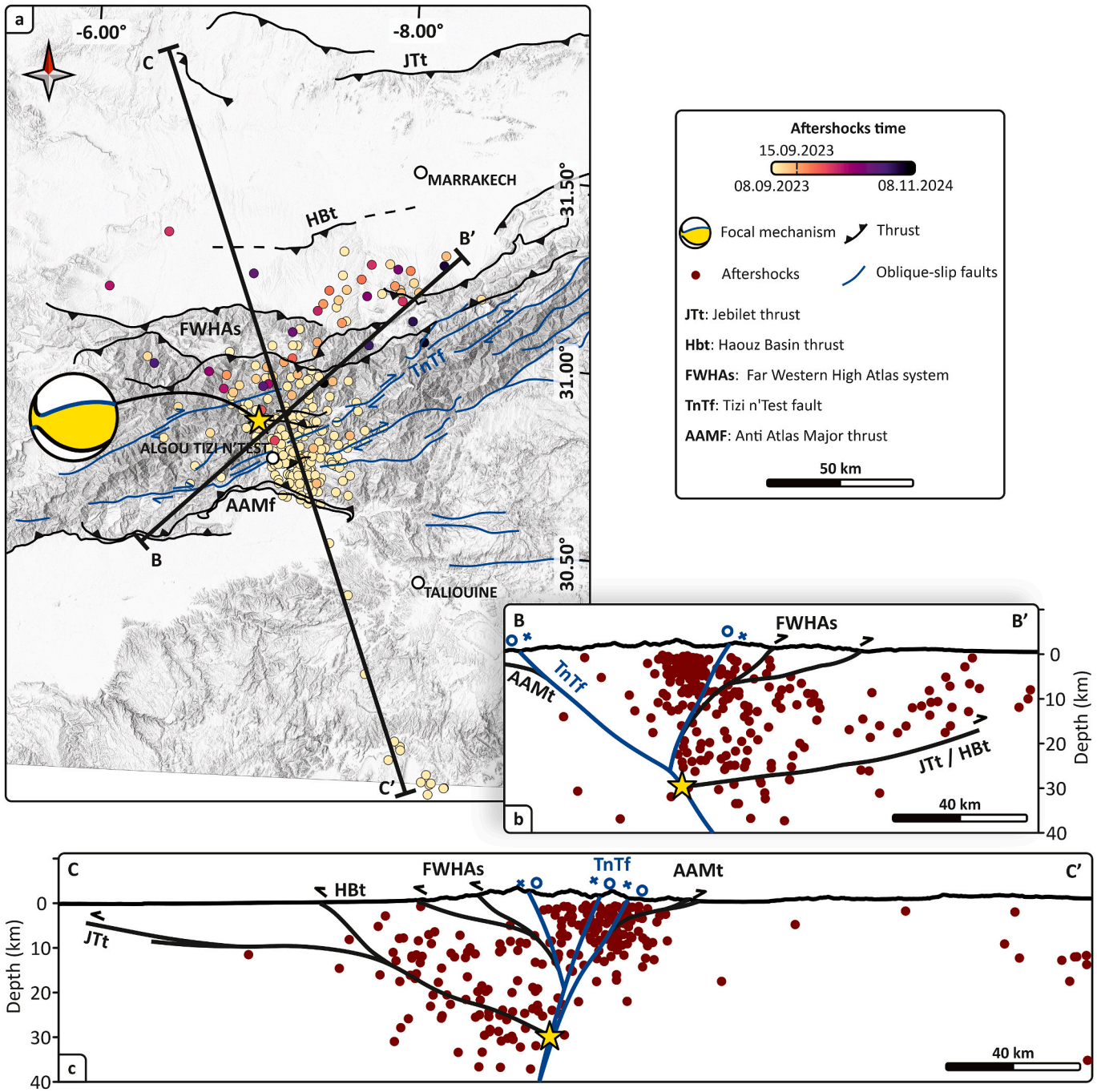

Fig. 2. Distribution of the re-localized aftershocks and the Mw 6.8 mainshock in map (**a**) and section views along two sections oriented in accordance to the seismicity distribution (**b**, **c**). In map view the seismicity is coloured based on the occurrence time.

that the horizontal component shows mainly the drift of the antiform flanks in the E-W direction. Therefore, the HDm does not represent a reliable coseismic deformation, being affected by the vertical component, and it is considered negligible.

4.3. TDE modelling

The first Triangular Elastic Dislocation (TDE) modelling solution, using simple planar fault geometries, involved two planes measuring 22 × 18 km each, with maximum slips of 2.4 m on the high-angle NNW-dipping plane and 2.6 m on the low-angle SW-dipping plane. The source is modelled at a depth of 28.3 km, corresponding to the planes' centroids (Fig. 4a and b) and calculated based on the USGS nodal planes (Table 2).

Residual analysis (Fig. S2) indicates that the modelled deformation field for the NNW-dipping plane is more consistent with the observed data compared to the SW-dipping plane. Most residuals are concentrated in the northwest, where the modelled vertical displacement (VD) slightly overestimates the observed DInSAR VD but still aligns well with the general dip of the antiform back limb, particularly for the NNW-dipping plane (Fig. 4).

In particular, the modelled deformation associated with the NNW-dipping plane (Fig. 4a) shows its maximum uplift slightly northeast of the mainshock, with most of the uplift concentrated north of the TnTf and less constrained by the FWHAs. These findings are consistent with the observed DInSAR VD (Fig. 3a). Conversely, the deformation modelled for the SW-dipping plane (Fig. 4b) indicates the highest uplift

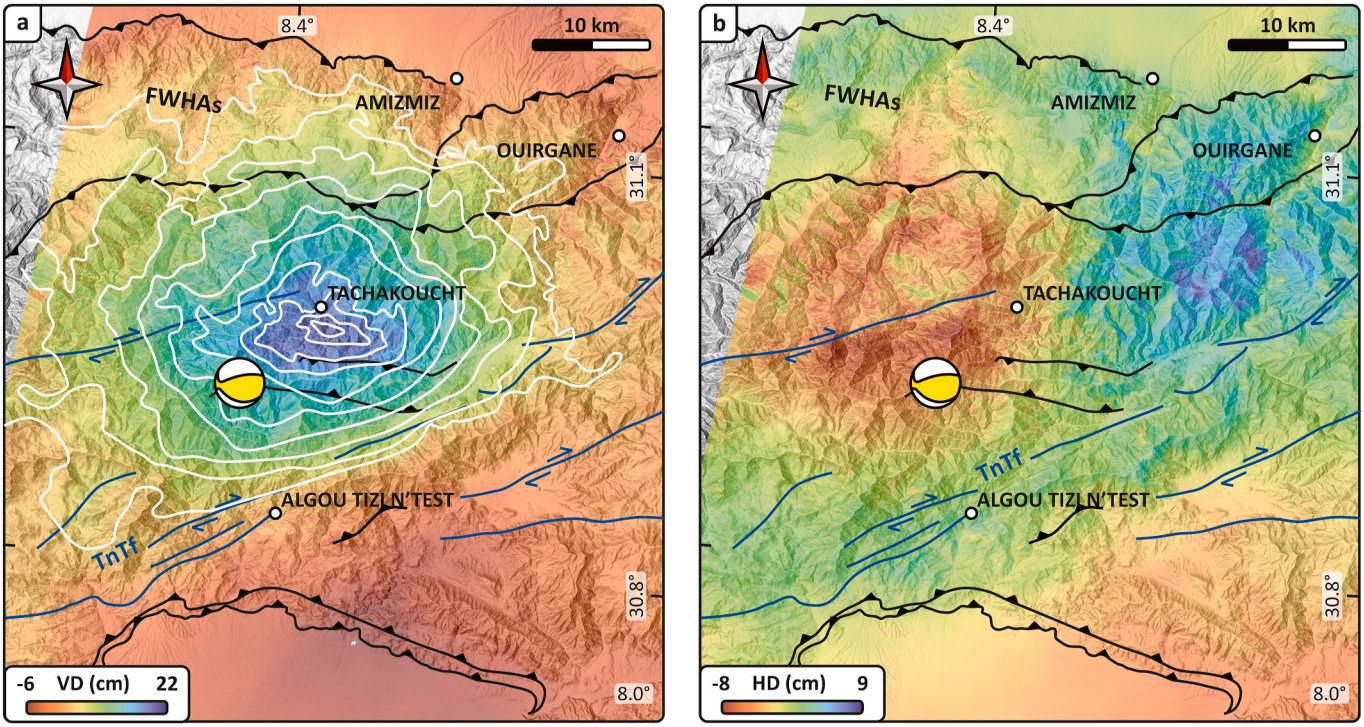

Fig. 3. Deformation field maps obtained from the DInSAR technique, showing the vertical (Equipotential displacement contours are shown in white) (**a**) and the E-W (**b**) components.

slightly northwest of the mainshock, with the entire deformation field shifted further west. Most of the uplift is concentrated between the Tizi n'Test fault (TnTf) and, to a lesser extent, the FWHAs, showing weaker consistency with the observed DInSAR VD (Fig. S2).

The analysis of the three differently oriented profiles (Fig. 4c–e) clearly shows that the NNW-dipping plane aligns more closely with the observed vertical displacement model (VDm) than the SW-dipping plane. Notably, the E-W oriented profile S4 (Fig. 4c) highlights a significant misfit in the deformation field associated with the SW-dipping plane, with its maximum uplift quite far from the observed DInSAR VD. From the observation of the profiles, the modelled deformation in the north tends to dip generally shallower than the observed DInSAR VD. Furthermore, it is noteworthy that if the modelled planes, which are confined at depth, were extrapolated to the surface, they would not align with any of the main outcropping reverse or transpressive faults.

The primary recognized tectonic structures in the epicentre area, consistent with the nodal planes and the mainshock location, are the JTt, its splay HBt and the TnTf (Fig. 1b). Being the seismicity in the shallow northern part well confined by the HBt, which splays out from a ramp of the JTt, and the modelled slip confined at depths, below the HBt detachment, we model them together and refer only to the JTt. Residual analysis (Fig. S3) conducted for both fault models shows that the deformation field modelled for the TnTf aligns more closely with the observed data than that of the JTt. Most residuals are concentrated in the northwestern region, where the modelled VD overestimates the observed DInSAR VD. For the JTt, the residuals reveal an evident misfit, with the modelled deformation field exhibiting significant shift compared to the DInSAR VD (Fig. S3). In contrast, the TnTf model demonstrates better agreement with DInSAR observations, albeit with slightly higher values in the northern area. The modelled deformation associated with the TnTf (Fig. 5a) shows its highest uplift values slightly northeast of the mainshock, with the deformation well constrained to the south by the TnTf but less to the north by the FWHAs. In contrast, the deformation modelled for the JTt (Fig. 5b) is poorly aligned with the observed DInSAR VD. Its uplift is positioned north-eastward, oriented NW-SE, and is neither well constrained by the TnTf nor the FWHAs. The subsidence, located to the WSW, is significantly shifted relative to the observed DInSAR subsidence.

To achieve the best fit for the vertical deformation, both fault surfaces are modelled with a larger slip area than the simple planar configuration (Table 2). The slip amount for the TnTf remains similar, while it is significantly higher for the JTt. The modelled slip area and slip amount for the TnTf are consistent with established scaling relationships (e.g., Leonard, 2014; Wells and Coppersmith, 1994) and result in a moment magnitude (M_o) of $2.2 \bullet 10^{19}$, which, following Cheloni et al. (2024), corresponds to a M_w of 6.8.

Conversely, the JTt's modelled slip area and amount are inconsistent with scaling ratios and a M_w of 6.8, yielding a M_o of $1.2 \bullet 10^{20}$, which, following Cheloni et al. (2024), would be equivalent to a M_w of 7.2. The best-fit modelled slip areas for both faults have an elliptical shape, aligning with the rake orientation defined by the USGS and consistent with the likely slip direction (Fig. 5c and d). The slip area modelled for the TnTf is widest in its lower section (below the mainshock), with its long axis oriented ENE (Fig. 5c), which effectively represents an upward propagating reverse slip. In contrast, the slip area for the JTt is more rounded and elongated downwards, with its maximum width above the mainshock, and its long axis ESE oriented (Fig. 5d).

If reverse slip movement is assumed, an elongated slip area directed downward along the fault would be inconsistent with this configuration. The three selected sections (Fig. 5e–g) emphasize the good fit of the modelled TnTf and the inconsistencies observed in the modelled JTt. Along all three sections, the modelled vertical displacement (VD) of the TnTf aligns well with the observed DInSAR VD, particularly in terms of the maximum uplift location and the overall dip of the antiform limbs, which correspond to a SSE-verging asymmetric fold. In contrast, the VD modelled for the JTt resembles a more symmetric antiform. Although the uplift is similar, the subsidence pattern significantly diverges from the observed data.

4.4. Coulomb stress change

Based on the aftershocks distribution, the DInSAR VDm and the TDE

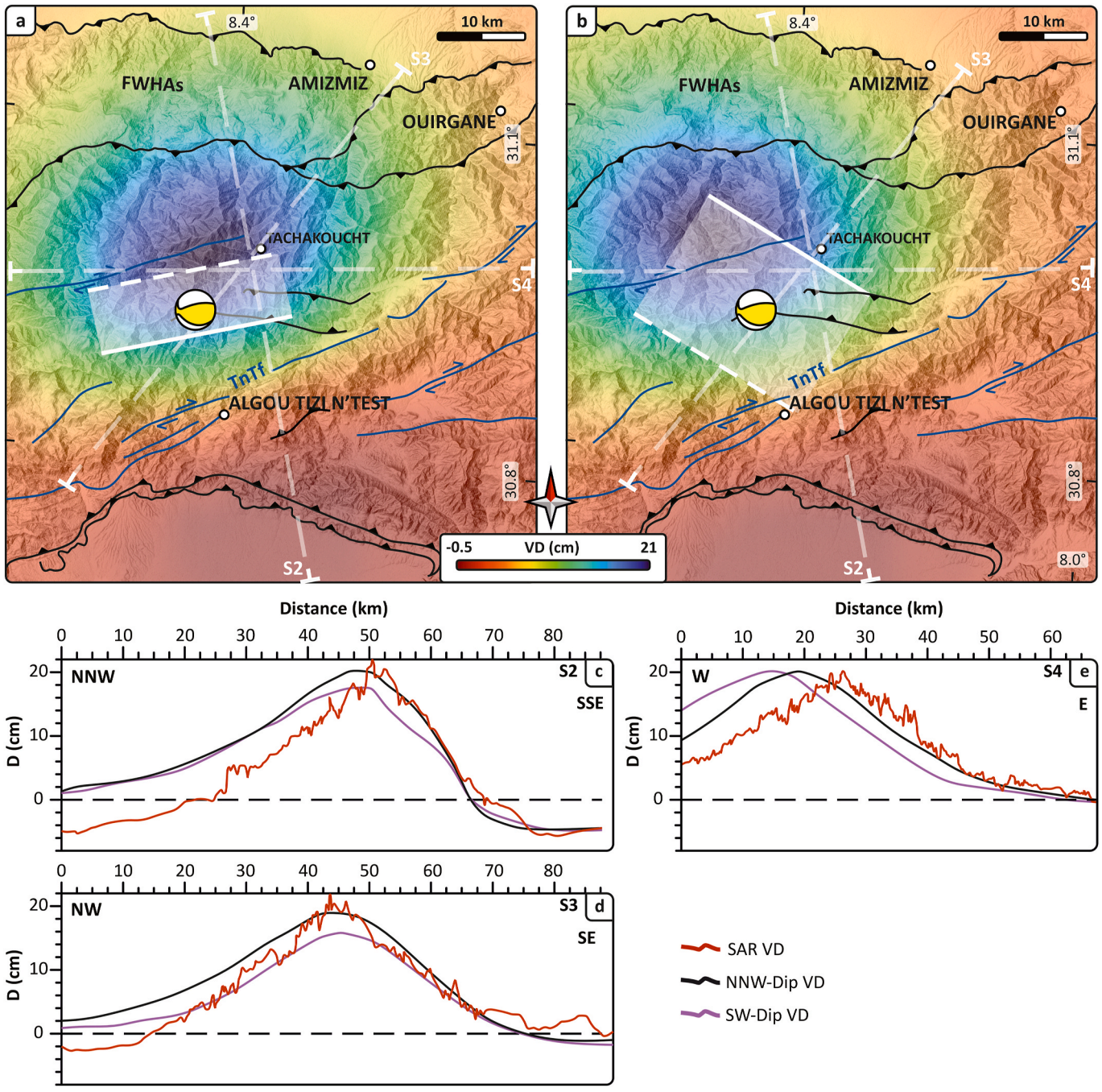

Fig. 4. Vertical displacement maps obtained from the TDE of the modelled high-angle NNW-dipping plane (**a**) and low-angle SW-dipping plane (**b**), also shown along the NNW-SSE oriented S2 (c), the NW-SE oriented S3 (d) and the E-W oriented S4 (**e**).

results, we are already confident to exclude a likely main seismogenic activity of the JTt; therefore, the Coulomb stress change is displayed only for the TnTf (Fig. 6), also including further 3 sections (Fig. S4). The Coulomb stress calculation for the JTt is shown in Fig. S5. The Coulomb stress calculation is a result of the TDE modelling and shows, as expected, a stress drop in correspondence with the modelled slip area and a stress rise at its tips (Fig. 6a). In general, the aftershocks are well distributed with respect to the stress rise lobes induced by the TnTf activity (Fig. 6a). Given a slip amount which decreases away from the mainshock, the Coulomb stress change is minimal at 0 km b.s.l., being comprised between −1 and 2.1 bar (Fig. 6b). At 5 km depth (Fig. 6c) the stress change increases reaching −2.3 and 5.3 bar; the aftershocks located between 0 and 5 km depth are distributed within lobes of both stress drop and rise, in proximity of the TnTf. In the northeast, a few aftershocks are located within a northeast propagating branch of the stress rise lobe; in the south, a couple of isolated aftershocks occur within an area of slight stress rise. At 15 km depth (Fig. 6d), the stress drop is the double of the stress rise, however we observe a wider stress rise distribution, in good agreement with the aftershocks. Further aftershocks occur both in the northeast and southeast, in correspondence with distributed slight stress rise. A couple of aftershocks also occur in the northwest, in accordance with a propagating stress rise lobe. At 25 km depth (Fig. 6e), which corresponds ca. to the mainshock depth, there is strong stress drop decrease, reaching −23.6 bar, surrounded by a wide stress rise area, which reaches 8.1 bar. A new set of aftershocks occur just north of the TnTf, within the stress rise lobe.

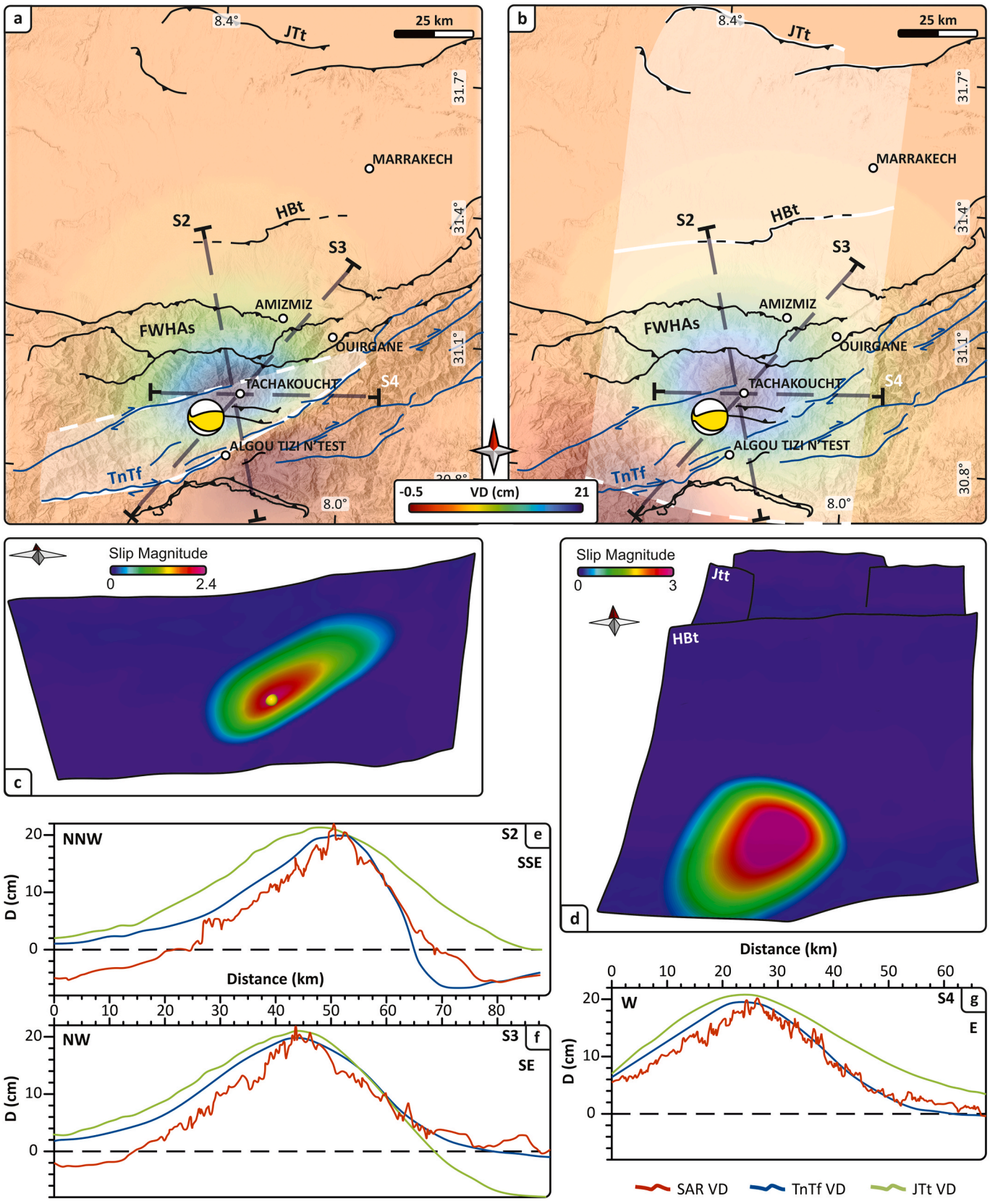

Fig. 5. Vertical displacement maps obtained from the TDE of the modelled TnTf (**a**) and JTt (**b**), also shown along the NNW-SSE oriented S2 (**c**), the NW-SE oriented S3 (**d**) and the E-W oriented S4 (**e**).

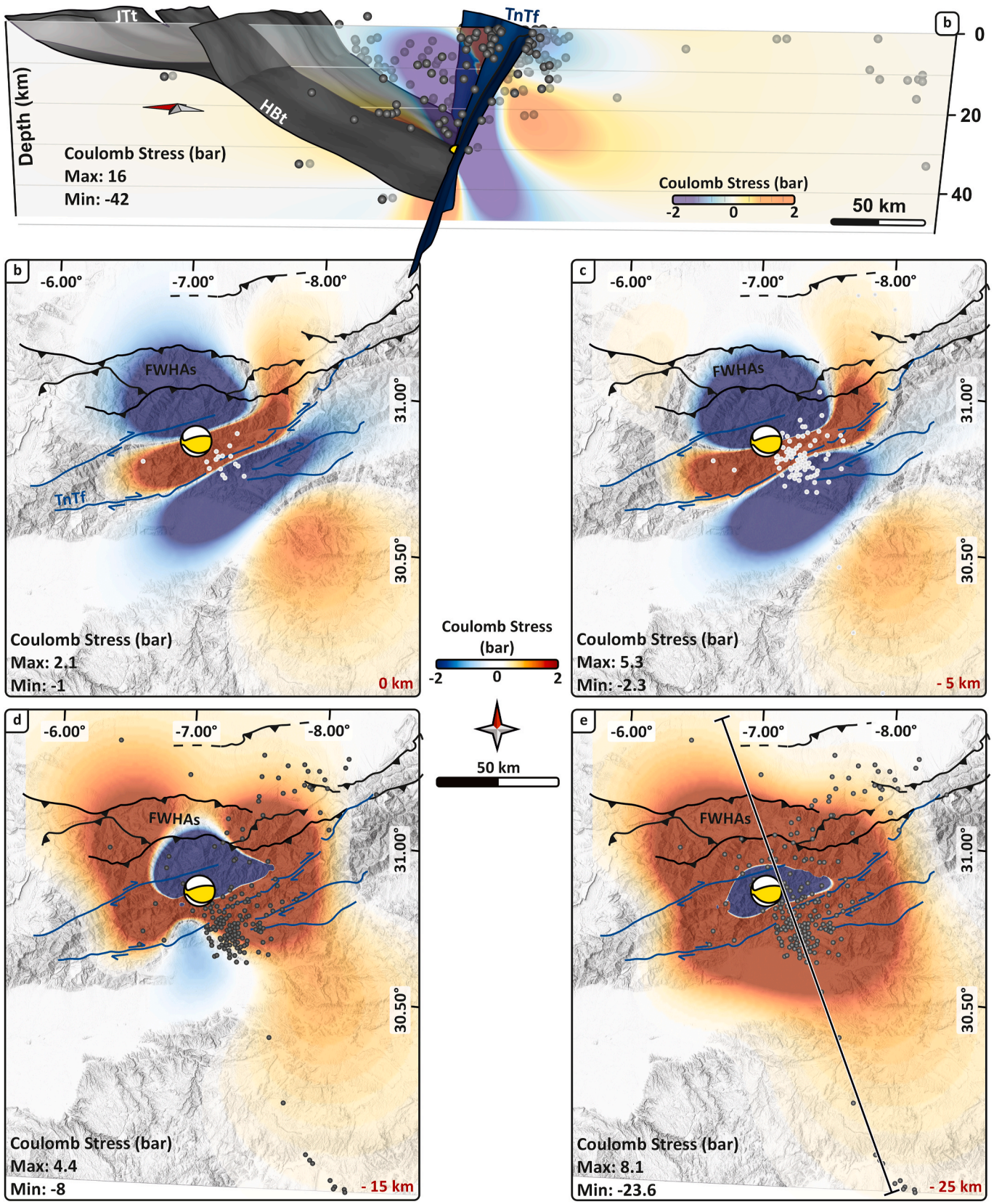

Fig. 6. (**a**) Section orthogonally oriented to the TnTf and parallel to the southern distribution of the seismicity (white and black dots), displaying the JTt and the vertical distribution of the Coulomb stress change induced by the TnTf. The Coulomb stress change related to the modelled seismogenic activity of the TnTf is shown at different depths, from 0 km (**b**), 5 km (**c**), 15 km (**d**) to 25 km (**e**). The aftershocks are visualized as both white and black dots.

5. Discussion and conclusions

The integration of existing geological data, DInSAR coseismic deformation, re-localized mainshock and aftershocks distribution, TDE modelling, and Coulomb stress change, reveals a complex seismological framework associated with the 2023 Mw 6.8 Al-Haouz earthquake and the WHA of Morocco.

The epicentral area is characterized by several transpressive and thrust faults, simultaneously active to partition the stress originated by the oblique relative movement of the African Plate with respect to the Eurasian Plate (e.g., DeMets et al., 1994, 2015; Dewey et al., 1989, Ellero et al., 2012; Lanari et al., 2020a,b; Serpelloni et al., 2007). Among them, the TnTf and the JTt have been identified as potential causative faults based on the mainshock location and focal mechanism. Our DInSAR observations and TDE modelling discard the possibility of the JTt as the causative fault for the mainshock, but suggest a most likely activity of the TnTf system. While previous studies have suggested this interpretation, relying on simplified planar fault models or geodetic and field data (Yeck et al., 2023; Huang et al., 2024; Nouayti et al., 2024; Skikra et al., 2025a; Touati et al., 2024), we strengthen this hypothesis by applying TDE modelling to complex and more comprehensive geometries accounting for two of the major existing structures: the TnTf and the JTt. However, we suggest that such an interpretation can only partially fit the observations and that the seismotectonic framework of the WHA is more complex, probably involving the activity of more faults. Malusà et al. (2024) already suggested the possible presence of a relatively newly formed blind structure which would link existing faults, responsible for the mainshock; the authors suggest that the activation of both a low-angle south-west-dipping structure, such as the one suggested by Cheloni et al. (2024), and an existing high-angle NW-dipping fault, such as the TnTf, would be difficult. However, the possibility to activate the no-optimal oriented TnTf is already discussed in literature (Levandowski, 2023; Huang et al., 2024; Skikra et al., 2025a); the authors suggest how the anomalously thin lithosphere and corresponding

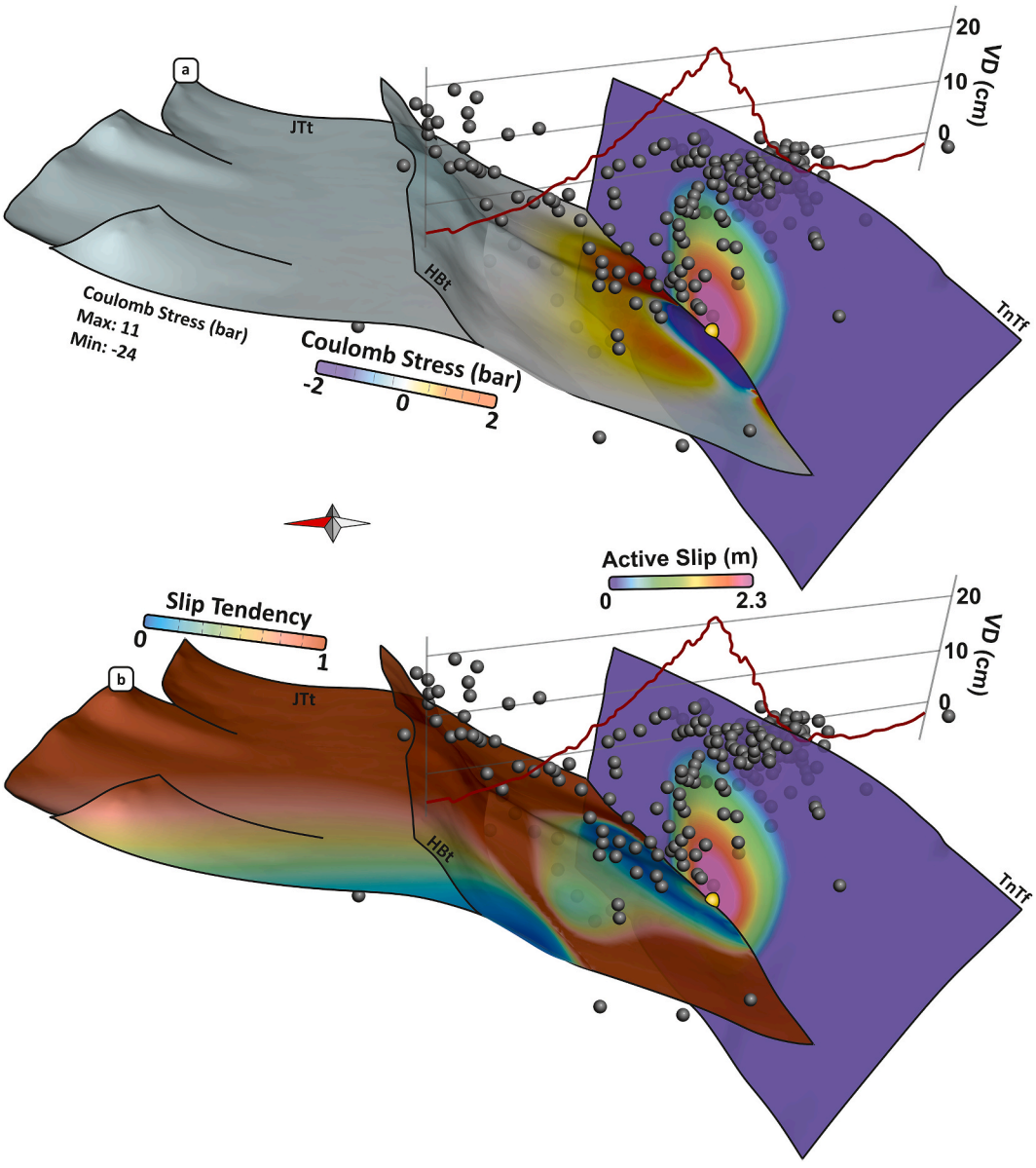

Fig. 7. Integrated 3D models showing the DInSAR VD (red line), the 3D aftershocks distribution (black dots) and the 3D models of the TnTf, the JTt and its splay HBt. The JTt and the HBt are shown with colours representing the Coulomb stress change (**a**) and the slip tendency (**b**) in response to the movement of the TnTf. The latter is shown with colours representing the amount of slip and its gradient in both panels (**a**, **b**). (For interpretation of the references to colour in this figure legend, the reader is referred to the Web version of this article.)

thermal mechanisms may favour fault weakening. Indeed, earthquake enucleation at great depths and high temperatures is observed worldwide, even if related to high strain rate areas (Molnar, 2020). Conversely the JTt is a optimal oriented structure, with a low dip angle, which may be easily reactivated in compression (Levandowski, 2023).

In this framework we suggest a new seismotectonic interpretation, in which both the TnTf and the JTt were activated during the earthquake sequence, consistently with Nouayti et al. (2024). The mainshock was promoted by the activation of the TnTf, whose slip of up to 2.3 m, caused a significant change of the stress field in the surrounding area. Such a stress field modification promoted the occurrence of the aftershocks close to the TnTf and mainly in the south, but also induced further stress to the JTt. The latter, being optimally oriented, slipped and promoted the occurrence of the sparse aftershocks cluster in the northeast. The mutual activity of both faults is also well suggested by the aftershocks spatial and temporal distribution; they tends to migrate northwards during the days and months following the mainshock and are mainly distributed in a triangular zone delimited by the TnTf and the JTt (Fig. 2).

To demonstrate this, we ingest the 3D surface of the JTt in the TDE modelling as a weaker passive structure to calculate both the induced Coulomb stress change and its slip tendency, in response to the active movement of the TnTf (Fig. 7) and its induced stress field. The results indicate that the induced Coulomb stress drop corresponds to a very low slip tendency in proximity of the slip area on the TnTf, along the JTt. Conversely, a Coulomb stress rise at the tips of the TnTf slip area is associated with a high slip tendency. The slip tendency distribution along the JTt shows how the fault system may be locked towards the northwest, while more free to slip towards the northeast. Considering that the Coulomb stress change given by a slip of the JTt would be consistent with the northeastern distribution of the aftershocks (Fig. S5), we suggest that the seismogenic activation of the TnTf affected, in a relatively later stage, the JTt, which slipped towards the northeast, promoting the occurrence of the aftershocks in the northeast.

The hypothesis of a near-synchronous activity of both an transpressive fault and a thrust in the WHA is in perfect agreement with the observed strain partitioning due to oblique convergence (e.g., DeMets et al., 1994, 2015; Dewey et al., 1989; Ellero et al., 2012; Lanari et al., 2020a,b; Serpelloni et al., 2007). Such strain partitioning can facilitate dynamic interactions between distinct fault systems, particularly in regions with oblique convergence as the Western High Atlas (WHA) of Morocco. Here, east-west striking transpressive faults with dips steeper than ~55° are generally less prone to reactivation under the dominant NNW-SSE compressive regime. This limitation arises from the unfavourable orientation of the principal stress axis (σ1) relative to the fault plane and the higher effective normal stress acting on these steeply dipping structures. High-angle reverse / transpressive faults (> 55° dip), such as the TnTf, require significantly higher shear stress to overcome their effective normal stress and initiate slip. This mechanical inefficiency under compressional regimes makes such faults less likely to experience significant seismic activity unless external factors, such as stress transfer from adjacent faults, low friction or high fluid pressure, alter the stress field (e.g., Sibson, 2012; Sibson and Xie, 1998). In cases where high-angle reverse faulting occurs, accumulated stress may partition onto conjugate and/or near faults.

These structures, having a more favourable orientations, accommodate deformation more efficiently. For example, in the WHA, the TnTf activity could promote stress redistribution to nearby faults such as the JTt and its splay HBt. This behaviour agrees with the principles of strain partitioning, where oblique convergence induces complementary fault systems to collectively accommodate tectonic deformation. This interplay between steep reverse faults and other more favourable systems underscores the complexity of strain distribution in the WHA and highlights the role of fault interactions in shaping the region's seismotectonic framework.

The interpretation of dominant long-term activity along the TnTf and a more subsidiary role for the JTt is also supported by geological and geomorphological evidence, including topography, drainage network, cooling ages and exhumation rates (Babault et al., 2008; Lanari et al., 2020a, 2020b). Such evidences demonstrate how the topography tends to be steeper in the southern flank of the WHA (i.e., south of the TnTf), which is reflected in a steeper drainage network; further to that, the exhumation rates are faster in proximity of the TnTf than in correspondence of the JTt and HBt. These evidences suggest that the 2023 Al-Haouz earthquake may represent a critical step in the long-term tectonic evolution of the WHA. The event highlights the importance of the TnTf in shaping the structural and topographic asymmetry of the region while highlighting the complex interplay of fault systems in accommodating oblique plate convergence.

Besides the modelling of the TnTf is in good agreement with remote sensing data and field observations, there may be still one point of open discussion. The vertical deformations calculated from the TDE modelling for all faults, are at least slightly shifted respect to the DInSAR VD and characterized by higher deformation in the north portion (Figs. S2 and S3). Besides the first order good agreement between the observed DInSAR VD and the modelled TnTf VD, we believe that the surface deformation could have been affected by the synchronous activity of further faults present in the area. Among these, the FWHAs and the transpressive faults south of the TnTf (Fig. 1) may be the best candidates. Further research is currently ongoing to characterize a possible synchronous activity of these faults.

CRediT authorship contribution statement

F. Carboni: Writing – review & editing, Writing – original draft, Visualization, Validation, Methodology, Investigation, Formal analysis, Conceptualization. **M. Occhipinti:** Writing – review & editing, Writing – original draft, Visualization, Validation, Software, Methodology, Investigation, Formal analysis, Data curation. **R. Lanari:** Writing – review & editing, Writing – original draft, Visualization, Validation, Investigation, Formal analysis, Conceptualization. **F. Medina:** Writing – review & editing, Validation, Data curation. **T.-E. Cherkaoui:** Data curation. **R. Gaspari:** Writing – review & editing, Validation, Software, Methodology, Investigation. **C. Faccenna:** Writing – review & editing, Validation, Investigation. **C. Chiarabba:** Writing – review & editing, Validation. **M. Porreca:** Writing – review & editing, Writing – original draft, Validation, Methodology, Investigation, Formal analysis, Conceptualization.

Declaration of competing interest

We state that this manuscript contains original results, data, ideas and/or interpretations not previously published or under consideration for publication elsewhere (including electronic media and databases).

The authors declare that they have no known competing financial interests or personal relationships that could have appeared to influence the work reported in this paper.

Acknowledgements

We thank the Editor, one anonymous reviewer and Simone Bello for their useful comments, which strongly improved the manuscript. This research was funded by Ministero dell'Istruzione dell'Università della Ricerca (MIUR) through the program PON "Ricerca e Innovazione" 2014–2022, the ASI-UniPG agreement 2019-2-HH, Fondo Ricerca 2022 Dip. Fisica e Geologia dell'Università di Perugia "A new approach to detect ground deformation after large earthquakes using open-source DInSAR data" (RICBAS2022PORRECA) and Fondo Ricerca Ateneo 2021 (WP3.1 "Disastri e Crisi Complesse). RL was supported by the Swiss National Science Foundation (SNSF) Sinergia Project MIGRATE - MIGRATE - A Multidisciplinary andInteGRated Approach for geoThermal Exploration - grant number 209434'. The TDE modelling

and Coulomb stress calculations were performed using the Fault Response Modelling module in the Move software (PE Limited) under academic licenses.

Appendix A. Supplementary data

Supplementary data to this article can be found online at https://doi.org/10.1016/j.jsg.2025.105394.

Data availability

Data will be made available on request.

References

Arboleya, M.L., Teixell, A., Charroud, M., Julivert, M., 2004. A structural transect through the high and middle atlas of Morocco. J. Afr. Earth Sci. 39 (3–5), 319–327. https://doi.org/10.1016/j.jafrearsci.2004.07.036.

Arboleya, M.L., Babault, J., Owen, L.A., Teixell, A., Finkel, R.C., 2008. Timing and nature of Quaternary fluvial incision in the Ouarzazate foreland basin, Morocco. J. Geol. Soc. 165 (6), 1059–1073. https://doi.org/10.1144/0016-76492007-151.

Babault, J., Teixell, A., Arboleya, M.L., Charroud, M., 2008. A late Cenozoic age for long-wavelength surface uplift of the Atlas Mountains of Morocco. Terra Nova 20 (2), 102–107. https://doi.org/10.1111/j.1365-3121.2008.00794.x.

Balestrieri, M.L., Moratti, G., Bigazzi, G., Algouti, A., 2009. Neogene exhumation of the Marrakech High Atlas (Morocco) recorded by apatite fission-track analysis. Terra Nova 21 (2), 75–82. https://doi.org/10.1111/j.1365-3121.2008.00857.x.

Barbero, L., Jabaloy, A., Gómez-Ortiz, D., Pérez-Peña, J.V., Rodríguez-Peces, M.J., Tejero, R., et al., 2011. Evidence for surface uplift of the Atlas Mountains and the surrounding peripheral plateaux: combining apatite fission-track results and geomorphic indicators in the Western Moroccan Meseta (coastal Variscan Paleozoic basement). Tectonophysics 502 (1–2), 90–104. https://doi.org/10.1016/j.tecto.2010.01.005.

Barchi, M.R., Carboni, F., Michele, M., Ercoli, M., Giorgetti, C., Porreca, M., Azzaro, S., Chiaraluce, L., 2021. The influence of subsurface geology on the distribution of earthquakes during the 2016–2017 Central Italy seismic sequence. Tectonophysics 807, 228797. https://doi.org/10.1016/j.tecto.2021.228797.

Beauchamp, W., Barazangi, M., Demnati, A., El Alji, M., 1996. Intracontinental rifting and inversion: missour basin and atlas mountains, Morocco. AAPG (Am. Assoc. Pet. Geol.) Bull. 80 (9), 1459–1481.

Bello, S., Lavecchia, G., Andreacci, C., Ercoli, M., Cirillo, D., Carboni, F., Barchi, M.R., Brozzetti, F., 2022. Complex trans-ridge normal faults controlling large earthquakes. Sci. Rep. 12, 10676. https://doi.org/10.1038/P41598-022-14406-4.

Bensaid, I., Cherkaoui, T.-E., Medina, M., Caldeira, B., Buforn, E., Emran, A., Hahou, Y., 2011. The 1992 Tafilalt seismic crisis (Anti-Atlas, Morocco). J. Seismol. 16, 35–53. https://doi.org/10.1007/s10950-011-9248-5.

Bignami, C., Valerio, E., Carminati, E., Doglioni, C., Tizzani, P., Lanari, R., 2019. Volume unbalance on the 2016 Amatrice-Norcia (Central Italy) seismic sequence and insights on normal fault earthquake mechanism. Sci. Rep. 9 (1), 4250. https://doi.org/10.1038/s41598-019-40958-z.

Bondár, I., Timoulali, Y., Chiang, A., Hni, L., Kasmi, M., 2024. Relocation of the 8 september 2023 high atlas, Morocco, earthquake aftershock sequence. Bull. Seismol. Soc. Am. https://doi.org/10.1785/0120240100.

Bouiflane, M., Le Corvec, N., Manar, A., Lanari, R., 2024. Spatial distribution and structural analysis of the Neogene Siroua volcanic field (Moroccan Atlas Mountains). Volcanica 7 (2), 835–851.

Burgmann, R., Ergintav, S., Segall, P., Hearn, E.H., McClusky, S., Reilinger, R.E., Woith, H., Zschau, J., 2002. Deformation during the 12 november 1999 duzce, Turkey, earthquake, from GPS and InSAR data. Bull. Seismol. Soc. Am. 92, 161–171. https://doi.org/10.1785/0120000834.

Carboni, F., Mirabella, F., Minelli, G., Saleh, H., Porreca, M., Ercoli, M., Pauselli, C., Barchi, M.R., 2024. Kinematic reconstruction of active tectonic and halokinetic structures in the 2021 NW Palagruza earthquake area (Central Adriatic). J. Struct. Geol. 182, 105112. https://doi.org/10.1016/j.jsg.2024.105112.

Carboni, F., Porreca, M., Valerio, E., Mariarosaria, M., De Luca, C., Azzaro, S., Ercoli, M., Barchi, M.R., 2022. Surface ruptures and off-fault deformation of the October 2016 central Italy earthquakes from DInSAR data. Sci. Rep. 12 (1), 3172. https://doi.org/10.1038/s41598-022-07068-9.

Cheloni, D., Famiglietti, N.A., Tolomei, C., Caputo, R., Vicari, A., 2024. The 8 September 2023, MW 6.8, Morocco earthquake: a deep transpressive faulting along the active high Atlas Mountain belt. Geophys. Res. Lett. 51 (2), 2023GL106992. https://doi.org/10.1029/2023GL106992.

Cherkaoui, T.-E., 1991. Contribution à l'étude de l'aléa sismique au Maroc. Joseph Fourier University, Grenoble, p. 246. PhD thesis. http://www.theses.fr/1991GRE10064.

Cherkaoui, T.-E., El Hassani, A., 2012. Seismicity and seismic hazard in Morocco. Bulletin de l'Institut Scientifique, Rabat, section Sciences de la Terre 34, 45–55.

Cherkaoui, T., Medina, F., 1988. Révision des données macrosismiques et du mécanisme au foyer du séisme d' Agadir du 29 février 1960. Rev. Geogr. Maroc 12, 51–61.

Clementucci, R., Ballato, P., Siame, L.L., Faccenna, C., Racano, S., Torreti, G., Lanari, R., Leanni, L., Guillou, V., 2023. Transient response to changes in uplift rates in the northern Atlas-Meseta system (Morocco). Geomorphology 436, 108765. https://doi.org/10.1016/j.geomorph.2023.108765.

Clementucci, R., Ballato, P., Siame, L.L., Fox, M., Lanari, R., Sembroni, A., Faccenna, C., Yaaqoub, A., Essaifi, A., 2024. Surface uplift and topographic rejuvenation of a tectonically inactive range: insights from the anti-atlas and the siroua massif (Morocco). Tectonics 42 (2), e2022TC007383. https://doi.org/10.1029/2022TC007383.

Delcaillau, B., Amrhar, M., Namous, M., Laville, E., Pedoja, K., Dugué, O., 2011. Transpressional tectonics in the Marrakech High Atlas: insight by the geomorphic evolution of drainage basins. Geomorphology 134 (3–4), 344–362. https://doi.org/10.1016/j.geomorph.2011.07.010.

DeMets, C., Gordon, R.G., Argus, D.F., Stein, S., 1994. Effect of recent revisions to the geomagnetic reversal time scale on estimates of current plate motions. Geophys. Res. Lett. 21 (20), 2191–2194. https://doi.org/10.1029/94GL02118.

DeMets, C., Iaffaldano, G., Merkouriev, S., 2015. High-resolution Neogene and quaternary estimates of Nubia-Eurasia-North America plate motion. Geophys. J. Int. 203 (1), 416–427. https://doi.org/10.1093/gji/ggv277.

Dewey, J.F., Helman, M.L., Knott, S.D., Turco, E., Hutton, D.H.W., 1989. Kinematics of the western mediterranean. Geol. Soc., London, Special Publications 45 (1), 265–283. https://doi.org/10.1144/GSL.SP.1989.045.01.15.

Dias, R., Hadani, M., Machado, I.L., Adnane, N., Hendaq, Y., Madih, K., Matos, C., 2011. Variscan structural evolution of the western High Atlas and the Haouz plain (Morocco). J. Afr. Earth Sci. 61 (4), 331–342. https://doi.org/10.1016/j.jafrearsci.2011.07.002.

Domènech, M., Teixell, A., Stockli, D.F., 2016. Magnitude of rift-related burial and orogenic contraction in the Marrakech High Atlas revealed by zircon (U-Th)/He thermochronology and thermal modeling. Tectonics 35 (11), 2609–2635. https://doi.org/10.1002/2016TC004283.

Duffaud, F., Rothé, J.P., Debrach, J., Erimesco, P., Choubert, G., Faure-Muret, A., 1962. Le séisme d'Agadir du 29 Février 1960. Notes & Mem. Serv. Géol. Maroc 154, 1–68.

Ellero, A., Ottria, G., Malusà, M.G., Ouanaimi, H., 2012. Structural geological analysis of the High Atlas (Morocco): evidence of a transpressional fold-thrust belt. Tectonics-Recent Adv. 229–258. https://doi.org/10.5772/50071.

Ellero, A., Malusà, G., Ottria, G., Ouanaimi, H., Froitzheimn, N., 2020. Transpressional structuring of the high Atlas belt, Morocco. J. Struct. Geol. 135, 104021. https://doi.org/10.1016/j.jsg.2020.104021.

Ercoli, M., Carboni, F., Akimbekova, A., Carbonell, R., Barchi, M.R., 2023. Evidencing subtle faults on deep seismic reflector profiles: data pre-conditioning and seismic attribute analysis on the Legacy CROP-04. Front. Earth Sci. 11. https://doi.org/10.3389/feart.2023.1119554.

Fekkak, A., Ouanaimi, H., Michard, A., Soulaimani, A., Ettachfini, E.M., Berrada, I., El Arabi, H., Lagnaoui, A., Saddiqi, O., 2018. Thick-skinned tectonics in a Late Cretaceous-Neogene intracontinental belt (High Atlas Mountains, Morocco): the flat-ramp fault control on basement shortening and cover folding. J. Afr. Earth Sci. 140, 169–188. https://doi.org/10.1016/j.jafrearsci.2018.01.008.

Ferranti, L., Carboni, F., Akimbekova, A., Ercoli, M., Bello, S., Brozzetti, F., Bacchiani, A., Toscani, G., 2024. Structural architecture and tectonic evolution of the Campania-Lucania arc (Southern Apennines, Italy): constraints from seismic reflection profiles, well data and structural-geologic analysis. Tectonophysics 879, 230313. https://doi.org/10.1016/j.tecto.2024.230313.

Frizon de Lamotte, D.F., Leturmy, P., Missenard, Y., Khomsi, S., Ruiz, G., Saddiqi, O., Guillocheau, F., Michard, A., 2009. Mesozoic and Cenozoic vertical movements in the Atlas system (Algeria, Morocco, Tunisia): an overview. Tectonophysics 475 (1), 9–28. https://doi.org/10.1016/j.tecto.2008.10.024.

Gabriel, A.K., Goldstein, R.M., Zebker, H.A., 1989. Mapping small elevation changes over large areas: differential radar interferometry. J. Geophys. Res. Solid Earth 94 (B7), 9183–9191. https://doi.org/10.1029/JB094iB07p09183.

Ghorbal, B., Bertotti, G., Foeken, J., Andriessen, P., 2008. Unexpected Jurassic to Neogene vertical movements in 'stable' parts of NW Africa revealed by low temperature geochronology. Terra Nova 20 (5), 355–363. https://doi.org/10.1111/j.1365-3121.2008.00828.x.

Gomez, F., Beauchamp, W., Barazangi, M., 2000. Role of the atlas mountains (northwest Africa) within the african-eurasian plate-boundary zone. Geology 28 (9), 775–778. https://doi.org/10.1130/0091-7613(2000)28<775:ROTAMN>2.0.CO;2.

Harris, R.A., 1998. Introduction to special section: stress triggers, stress shadows, and implications for seismic hazard. J. Geophys. Res. 103 (B10), 24347–24358.

Huang, K., Wei, G., Chen, K., Zhang, N., Li, M., Dal Zilio, L., 2024. The 2023 Mw 6.8 Morocco earthquake: a lower crust event triggered by mantle upwelling? Geophys. Res. Lett. 51 (12), 2024GL109052.

Jabour, N., Kasmi, M., Menzhi, M., Birouk, A., Hni, L., Hahou, Y., Timoulali, Y., Badrane, S., 2004. The February 24th, 2004 Al Hoceima Earthquake. Newsletter of European-Mediterranean Seismological Centre, p. 21.

Klein, F.W., 2002. In: User's Guide to HYPOINVERSE-2000, a Fortran Program to Solve for Earthquake Locations and Magnitudes, 1.37. U.S. Geol. Surv. Open-File Rep. 02-171 revised, p. 142. https://doi.org/10.3133/ofr02171.

Koulali, A., Ouazar, D., Tahayt, A., King, R.W., Vernant, P., Reilinger, R.E., McClusky, S., Mourabit, T., Davila, J.M., Amraoui, N., 2011. New GPS constraints on active deformation along the Africa–Iberia plate boundary. Earth Planet Sci. Lett. 308 (1–2), 211–217. https://doi.org/10.1016/j.epsl.2011.05.048.

Lanari, R., Berardino, P., Bonano, M., Casu, F., Manconi, A., Manunta, M., Manzo, M., Pepe, A., Pepe, S., Sansosti, E., Solaro, G., 2010. Surface displacements associated with the L'Aquila 2009 Mw 6.3 earthquake (central Italy): new evidence from SBAS-DInSAR time series analysis. Geophys. Res. Lett. 37 (20). https://doi.org/10.1029/2010GL044780.

Lanari, R., Fellin, M.G., Faccenna, C., Balestrieri, M.L., Pazzaglia, F.J., Youbi, N., Maden, C., 2020a. Exhumation and surface evolution of the western high atlas and

surrounding regions as constrained by low temperature thermochronology. Tectonics 39 (3), e2019TC005562. https://doi.org/10.1029/2019TC005562.
Lanari, R., Faccenna, C., Fellin, M.G., Essaifi, A., Nahid, A., Medina, F., Youbi, N., 2020b. Tectonic evolution of the western high Atlas of Morocco: oblique convergence, reactivation, and transpression. Tectonics 39 (3), e2019TC005563. https://doi.org/10.1029/2019TC005563.
Lanari, R., Boutoux, A., Faccenna, C., Herman, F., Willett, S.D., Ballato, P., 2023a. Cenozoic exhumation in the mediterranean and the Middle East. Earth Sci. Rev. 237, 104328. https://doi.org/10.1016/j.earscirev.2023.104328.
Lanari, R., Faccenna, C., Natali, C., Şengül Uluocak, E.B.R.U., Fellin, M.G., Becker, T.W., Göğüş, O.H., Youbi, N., Clementucci, R., Conticelli, S., 2023b. The Atlas of Morocco: a plume-assisted orogeny. G-cubed 24 (6), e2022GC010843. https://doi.org/10.1029/2022GC010843.
Lavecchia, G., Castaldo, R., de Nardis, R., De Novellis, V., Ferrarini, F., Pepe, S., Brozzetti, F., Solaro, G., Cirillo, D., Bonano, M., Boncio, P., Casu, F., De Luca, C., Lanari, R., Manunta, M., Manzo, M., Zinno, I., Tizzani, P., 2016. Ground deformation and source geometry of the 24 August 2016 Amatrice earthquake (Central Italy) investigated through analytical and numerical modelling of DInSAR measurements and structural-geological data. Geophys. Res. Lett. 43 (12), 389–398. https://doi.org/10.1002/2016GL071723.
Laville, E., Pique, A., 1991. La Distension crustale atlantique et atlasique au Maroc au début du Mésozoïque; le rejeu des structures hercyniennes. Bull. Soc. Geol. Fr. 162, 1161–1171.
Leonard, M., 2014. Self-consistent earthquake fault-scaling relations: update and extension to stable continental strike-slip faults. Bull. Seis. Soc. A. 104 (6), 2953–2965. https://doi.org/10.1785/0120140087.
Leprêtre, R., Missenard, Y., Barbarand, J., Gautheron, C., Saddiqi, O., Pinna-Jamme, R., 2015. Postrift history of the eastern central Atlantic passive margin: insights from the Saharan region of South Morocco. J. Geophys. Res. Solid Earth 120 (6), 4645–4666. https://doi.org/10.1002/2014JB011549.
Leprêtre, R., Missenard, Y., Barbarand, J., Gautheron, C., Jouvie, I., Saddiqi, O., 2018. Polyphased inversions of an intracontinental rift: case study of the marrakech high atlas, Morocco. Tectonics 37 (3), 818–841. https://doi.org/10.1002/2017TC004693.
Levandowski, W., 2023. Fault-Slip potential near the deadly 8 september 2023 Mw 6.8 Al Haouz, Morocco, earthquake. The Seismic Record 3 (4), 367–375. https://doi.org/10.1785/0320230037.
Malusà, M.G., Ellero, A., Ottria, G., 2024. Tectonics of the Mw 6.8 Al Haouz earthquake (Morocco) reveals minor role of asthenospheric upwelling. Tectonophysics 891, 230533. https://doi.org/10.1016/j.tecto.2024.230533.
Mancilla, F. de Lis, Diaz, J., 2015. High resolution Moho topography map beneath Iberia and Northern Morocco from receiver function analysis. Tectonophysics 663, 203–211. https://doi.org/10.1016/j.tecto.2015.06.017.
Massonnet, D., Feigl, K.L., 1998. Radar interferometry and its application to changes in the Earth's surface. Rev. Geophys. 36 (4), 441–500. https://doi.org/10.1029/97RG03139.
Mattauer, M., Proust, F., Tapponnier, P., 1972. Major strike-slip fault of late Hercynian age in Morocco. Nature 237 (5351), 160–162. https://doi.org/10.1038/237160b0.
McGuire, J.J., Segall, P., 2003. Imaging of a seismic fault slip transients recorded by dense geodetic networks. Geophys. J. Int. 155, 778–788. https://doi.org/10.1111/j.1365-246X.2003.02022.x.
Meade, B.J., 2007. Algorithms for the calculation of exact displacements, strains, and stresses for triangular dislocation elements in a uniform elastic half space. Comput. Geosci. 33, 1064–1075. https://doi.org/10.1016/j.cageo.2006.12.003.
Medina, F., El Alami, S.O., 2006. Focal mechanisms and state of stress in the Al Hoceima area (Central Rif, Morocco). Bulletin de l'Institut Scientifique 28, 19–30.
Medina, F., Cherkaoui, T.-E., 1991. Focal mechanisms of the Atlas earthquakes, and tectonic implications. Geol. Rundsch. 80 (3), 639–648. https://doi.org/10.1007/BF01803691.
Meghraoui, M., Outtani, F., Choukri, A., de Lamotte, D.F., 1999. Coastal tectonics across the South Atlas thrust front and the Agadir active zone, Morocco. Geol. Soc., London, Special Publications 146 (1), 239–253. https://doi.org/10.1144/gsl.sp.1999.146.01.14.
Missenard, Y., Zeyen, H., Frizon de Lamotte, D., Leturmy, P., Petit, C., Sébrier, M., Saddiqi, O., 2006. Crustal versus asthenospheric origin of relief of the Atlas Mountains of Morocco. J. Geophys. Res. Solid Earth 111 (B3). https://doi.org/10.1029/2005JB003708.
Missenard, Y., Taki, Z., de Lamotte, D.F., Benammi, M., Hafid, M., Leturmy, P., Sébrie, M., 2007. Tectonic styles in the Marrakesh High Atlas (Morocco): the role of heritage and mechanical stratigraphy. J. Afr. Earth Sci. 48, 247–266. https://doi.org/10.1016/j.jafrearsci.2007.03.007.
Missenard, Y., Saddiqi, O., Barbarand, J., Leturmy, P., Ruiz, G., El Haimer, F.Z., de Lamotte, D.F., 2008. Cenozoic denudation in the Marrakech high Atlas, Morocco: insight from apatite fission-track thermochronology. Terra Nova 20 (3), 221–228. https://doi.org/10.1111/j.1365-3121.2008.00810.x.
Molnar, P., 2020. The brittle-plastic transition, earthquakes, temperatures, and strain rates. JGR: Solid Earth 125, e2019JB019335. https://doi.org/10.1029/2019JB019335.
Mourabit, T., Abou Elenean, K.M., Ayadi, A., Benouar, D., Ben Suleman, A., Bezzeghoud, M., Cheddadi, A., Chourak, M., ElGabry, M.N., Harbi, A., Hfaiedh, M., Hussein, H.M., Kacem, J., Ksentini, A., Jabour, N., Magrin, A., Maouche, S., Meghraoui, M., Ousadou, F., Panza, G.F., Peresan, A., Romdhane, N., Vaccari, F., Zuccolo, E., 2014. Neo-deterministic seismic hazard assessment in North Africa. J. Seism. 18, 301–318. https://doi.org/10.1007/s10950-013-9375-2.
Nouayti, A., Moudnib, L.E., Khattach, D., Zeckra, M., Nouayti, N., Saadi, O., Elhairechi, K., Oujane, B., Iken, H., 2024. Seismic synthesis of the Al Haouz earthquake of September 8th, 2023 by integrating gravimetric and aeromagnetic data from the western High Atlas in Morocco. Model. Earth Syst. Environ. 1–20. https://doi.org/10.1007/s40808-024-02148-3.
Occhipinti, M., Carboni, F., Amorini, S., Paltriccia, N., López-Martínez, C., Porreca, M., 2024. Implementing the European space agency's SentiNel application platform's open-source Python module for differential synthetic aperture radar interferometry coseismic ground deformation from sentinel-1 data. Remote Sens. 16 (1), 48. https://doi.org/10.3390/rs16010048.
Okada, Y., 1985. Surface deformation due to shear and tensile faults in a half- space. Bull. Seismol. Soc. Am. 75 (4), 1135–1154. https://doi.org/10.1785/bssa0750041135.
Okada, Y., 1992. Internal deformation due to shear and tensile faults in a half-space. Bull. Seismol. Soc. Am. 82 (2), 1018–1040. https://doi.org/10.1785/BSSA0820021018.
Papadopoulos, G.A., Agalos, A., Karavias, A., Triantafyllou, I., Parcharidis, I., Lekkas, E., 2021. Seismic and geodetic imaging (DInSAR) investigation of the March 2021 strong earthquake sequence in Thessaly, central Greece. Geosci. 11 (8), 311. https://doi.org/10.3390/geosciences11080311.
Peláez, J.A., Chourak, M., Tadili, B.A., Brahim, L.A., Hamdache, M., Casado, C.L., Solares, J.M., 2007. A catalog of main Moroccan earthquakes from 1045 to 2005. Seismol Res. Lett. 78 (6), 614–621.
Porreca, M., Minelli, G., Ercoli, M., Brobia, A., Mancinelli, P., Cruciani, F., Giorgetti, C., Carboni, F., Mirabella, F., Cavinato, C., Cannata, A., Pauselli, C., Barchi, M.R., 2018. Seismic reflection profiles and subsurface geology of the area interested by the 2016–2017 earthquake sequence (Central Italy). Tectonics 37. https://doi.org/10.1002/2017TC004915.
Qin, Y., Tian, H., Xu, N.X., Chen, Y., 2020. Physical and mechanical properties of granite after high-temperature treatment. Rock Mech. Rock Eng. 53, 305–322. https://doi.org/10.1007/s00603-019-01919-0.
Savage, J.C., Burford, R.O., 1973. Geodetic determination of relative plate motion in central California. J. Geophys. Res. 78, 832–845.
Sébrier, M., Siame, L., Zouine, E.M., Winter, T., Missenard, Y., Leturmy, P., 2006. Active tectonics in the Moroccan high atlas. C. R. Geosci. 338 (1–2), 65–79. https://doi.org/10.1016/j.crte.2005.12.001.
Serpelloni, E., Vannucci, G., Pondrelli, S., Argnani, A., Casula, G., Anzidei, M., Baldi, P., Gasperini, P., 2007. Kinematics of the Western Africa-Eurasia plate boundary from focal mechanisms and GPS data. Geophys. J. Int. 169 (3), 1180–1200. https://doi.org/10.1111/j.1365-246X.2007.03367.x.
Sibson, R.H., 2012. Reverse fault rupturing: competition between non-optimal and optimal fault orientations. In: Healy, D., Butler, R.W.H., Ship-ton, Z.K., Sibson, R.H. (Eds.), Faulting, Fracturing and Igneous Intrusion in the Earth's Crust. Geol. Soc. Lond. Spec. Publ. 367. The Geological Society, London, United Kingdom, pp. 39–50.
Sibson, R.H., Xie, G., 1998. Dip range for intracontinental reverse fault ruptures: truth not stranger than friction? Seismol. Soc. Am. Bull. 88, 1014–1022.
Skikra, H., Fadil, A., Ouassanouan, Y., Lakhouidsi, K., Tahayt, A., Soulaimani, A., El Moudnib, L., 2025a. Seismotectonic assessment of the high atlas orogen: implications for the 8 september mw 6.8 el-haouz earthquake. Tectonophysics 895, 230573. https://doi.org/10.1016/j.tecto.2024.230573.
Skikra, H., Lanari, R., Soulaimani, A., Ouabid, M., Raji, O., 2025b. Spatiotemporal evolution of tectonic stresses during the High Atlas Cenozoic basin inversion: impact of plate kinematics and structural inheritance. Tectonics. https://doi.org/10.1029/2024TC008618.
Soumaya, A., Ben Ayed, N., Rajabi, M., Meghraoui, M., Delvaux, D., Kadri, A., Ziegler, M., Maouche, S., Braham, A., 2018. Active faulting geometry and stress pattern near complex strike-slip systems along the Maghreb region: constraints on active convergence in the Western Mediterranean. Tectonics 37 (9), 3148–3173. https://doi.org/10.1029/2018TC004983.
Spieker, K., Wölbern, I., Thomas, C., Harnafi, M., El Moudnib, L., 2014. Crustal and upper-mantle structure beneath the western Atlas Mountains in SW Morocco derived from receiver functions. Geophys. J. Internat.l 198 (3), 1474–1485. https://doi.org/10.1093/gji/ggu216.
Steacy, S., Gomberg, J., Cocco, M., 2005. Introduction to special section: stress transfer, earthquake triggering, and time-dependent seismic hazard. J. Geophys. Res. 110, B05S01. https://doi.org/10.1029/2005JB003692.
Teixell, A., Arboleya, M.L., Julivert, M., Charroud, M., 2003. Tectonic shortening and topography in the central High Atlas (Morocco). Tectonics 22 (5). https://doi.org/10.1029/2002TC001460.
Teixell, A., Ayarza, P., Zeyen, H., Fernàndez, M., Arboleya, M.L., 2005. Effects of mantle upwelling in a compressional setting: the Atlas Mountains of Morocco. Terra Nova 17 (5), 456–461. https://doi.org/10.1111/j.1365-3121.2005.00633.x.
Tesòn, E., Teixell, A., 2008. Sequence of thrusting and syntectonic sedimentation in the eastern Sub-Atlas thrust belt (Dades and Mgoun valleys, Morocco). Int. J. Earth Sci. 97, 103–113. https://doi.org/10.1007/s00531-006-0151-1.
Timoulali, Y., Meghraoui, M., 2011. 3-D crustal structure in the Agadir region (SW High Atlas, Morocco). J. Seismol. 15 (4), 625. https://doi.org/10.1007/s10950-011-9240-0. Springer Verlag.
Timoulali, Y., Nacer, J., Youssef, H., Mimoun, C., 2015. Lithospheric structure in NW of Africa: Case of the Moroccan Atlas MountainsAuthor links open overlay panel. Geodesy and Geodynamics 6 (6), 397–408. https://doi.org/10.1016/j.geog.2015.12.003.
Tondi, E., Blumetti, A.M., Čičak, M., Di Manna, P., Galli, P., Invernizzi, C., Mazzoli, S., Piccardi, L., Valentini, G., Vittori, E., Volatili, T., 2021. Conjugate coseismic surface faulting related with the 29 December 2020, Mw 6.4, Petrinja earthquake (Sisak-Moslavina, Croatia). Sci. Rep. 11 (1), 9150. https://doi.org/10.1038/s41598-021-88378-2.
Touati, B., Gu, W., Ni, S., Chu, R., Sheng, M., Xue, Q., Bellalem, F., Maouche, S., Yahyaoui, H., 2024. The 2023 M w 6.8 Adassil Earthquake (Chichaoua, Morocco) on

a steep reverse fault in the deep crust and its geodynamic implications. Earth Planet. Phys. 8 (3), 522. https://doi.org/10.26464/epp2024019.

Valerio, E., Manzo, M., Casu, F., Convertito, V., De Luca, C., Manunta, M., Monterroso, F., Lanari, R., De Novellis, V., 2020. Seismogenic source model of the 2019, mw 5.9, East-Azerbaijan earthquake (NW Iran) through the inversion of sentinel-1 DInSAR measurements. Remote Sens. 12 (8), 1346. https://doi.org/10.3390/rs12081346.

Wells, D.L., Coppersmith, K.J., 1994. New empirical relationships among magnitude, rupture length, rupture width, rupture area, and surface displacement. Bull. Seismol. Soc. Am. 84 (4), 974–1002.

Wu, W., Zhang, Y., Hao, X., Liu, J., 2024. The source kinematics and slip distribution of the 2023 Mw 6.8 Morocco earthquake. J. Afr. Earth Sci. 220, 105451. https://doi.org/10.1016/j.jafrearsci.2024.105451.

Yagi, Y., Okuwaki, R., Hirano, S., Enescu, B., Chikamori, M., Yamaguchi, R., 2024. Barrier-induced rupture front disturbances during the 2023 Morocco earthquake. Seismol Res. Lett. 95 (3), 1591–1598. https://doi.org/10.1785/0220230357.

Yeck, W.L., Hatem, A.E., Goldberg, D.E., Barnhart, W.D., Jobe, J.A.T., Shelly, D.R., Villaseñor, A., Benz, H.M., Earle, P.S., 2023. Rapid source characterization of the 2023 M w 6.8 Al Haouz, Morocco, earthquake. The Seismic Record 3 (4), 357–366. https://doi.org/10.1785/0320230040.

Zhang, J., Peng, C., Fu, J., Dong, G., Zhang, H., Cao, Q., Su, Y., 2024. Granite mechanical properties and SHPB testing in geothermal development: a review. Geoenergy Sci. Eng. 243, 213361. https://doi.org/10.1016/j.geoen.2024.213361.